Ductal carcinoma *in situ*: magnetic resonance and ultrasound imaging in mouse models of breast cancer

Sanaz A Jansen

Postdoctoral research conducted in the lab of Terry Van Dyke, Mouse Cancer Genetics Program, National Cancer Institute, Frederick National Laboratory for Cancer Research. This research project was conducted in collaboration with Lilia Ileva, Lisa Riffle, Lucy Lu, Miriam Anver, Joseph Kalen and Terry Van Dyke.

ABSTRACT

The earliest stage of breast cancer, ductal carcinoma *in situ* (DCIS), is a remarkably heterogeneous disease with diverse molecular and prognostic subtypes. Mouse models of breast cancer offer an effective experimental framework in which to investigate DCIS, and biomedical imaging can provide potential insights into the biology of these models. In this study, we develop a high resolution, multi-modality strategy for imaging preinvasive mammary neoplasias in two mouse models of DCIS. We performed high resolution magnetic resonance imaging (MRI) on a 3Tesla clinical scanner, using noncontrast T_1 and T_2 weighted acquisitions and dynamic contrast enhanced MRI. Preinvasive lesions were readily identified on noncontrast T_1 and T_2 weighted acquisitions. Subsequently, MRI-directed ultrasound was performed and an agar grid was used to correlate MRI with ultrasound and histology. We found that both MRI and ultrasound were able to detect preinvasive neoplasias with high sensitivity (over 90% in the posterior inguinal mammary glands). This study has established an imaging strategy for monitoring mouse models of DCIS, with rapid imaging acquisitions in two different modalities. We have also introduced a new method for correlating MRI with ultrasound and histology. This work sets the

stage for combining advanced imaging and mouse modeling techniques to gain relevant insights on

image-based biomarkers of DCIS.

INTRODUCTION

Ductal carcinoma *in situ* (DCIS) is a preinvasive breast cancer wherein neoplastic cells remain confined within the milk duct basement membrane. DCIS is a nonobligate precursor to invasive ductal carcinoma (IDC) and comprises 20-30% of newly diagnosed breast cancers in the US (Kerlikowske, 2010). It is a remarkably heterogeneous disease with distinct histological and molecular subtypes. These include nuclear grade (low, intermediate or high), gene-expression profiling patterns (luminal A, luminal B, basal or ERBB2) and alterations in regulators of cellular proliferation, apoptosis and genomic stability such as HER2, Rb and PTEN (Allred, 2010, Lari and Kuerer, 2011). Perhaps most relevant are the subtypes of DCIS with more aggressive growth, i.e., lesions that differentiate based on risk of progression to invasive carcinoma (Allegra et al., 2010). Indirect evidence suggests that a significant portion of DCIS lesions will never progress to an invasive, life-threatening carcinoma (Erbas et al., 2006). However, reliable identification of this subset of women with indolent disease who may benefit from less aggressive therapeutic interventions is not currently possible based on known histological or molecular characteristics (Allegra et al., 2010).

As a complementary approach, the capacity for *in vivo* imaging to provide a noninvasive characterization of DCIS biological and physical properties is an important goal (Jansen, 2011). Clinically, DCIS presents as calcifications on x-ray mammography in a variety of shapes and distributions (D'Orsi, 2010). On dynamic contrast enhanced MRI (DCEMRI) DCIS exhibits a distinctive nonmass-like morphology, with a diversity of distributions and internal enhancement patterns as described by the Breast Imaging and Reporting Data System (BIRADS) lexicon (Jansen et al., 2007). The contrast media uptake and washout, or kinetic, curves for DCIS usually exhibit a plateau or washout shape (Jansen et al., 2007). Breast ultrasound is a widely performed clinical imaging technique, most often utilized in a mammogram- or MRI-directed manner to further evaluate detected abnormalities (Abe et al., 2010). DCIS typically presents as a hypoechoic lesion with irregular shape and indistinct margins on ultrasound (Cho et al., 2011). Despite the widespread use of imaging in the management of DCIS, the association between image-based features and the underlying molecular and prognostic subtypes of DCIS is not well

understood. Studies of women with DCIS are hampered by several challenges including applying consistent imaging techniques in large cohorts of women, obtaining access to tissue specimens, and performing accurate radiologic-pathologic correlation.

Mouse models provide an appealing alternative experimental framework for investigating image-based biomarkers of DCIS because they, in principle, do not suffer from these limitations. As a further advantage, in genetically engineered mouse models (GEMMs), distinct genetic alterations can be targeted to the mammary epithelium in an experimentally controlled manner. These, in turn, have the potential to generate different molecular and prognostic subtypes of preinvasive cancer that can form the foundation for investigating imaging correlations (Van Dyke and Jacks, 2002). However, if mouse models are to serve as a test-bed for developing image-based molecular and prognostic biomarkers of DCIS, several technical advances are required. First, for the purpose of studying molecular, metabolic or physical imaging signatures, highly sensitive anatomic imaging techniques are essential for accurate lesion detection and localization. Second, it is critical to develop multimodality co-registration techniques that can register images with one another and with histology. In this study, we set out to address these goals. We have developed and validated an MRI and ultrasound imaging approach for characterizing preinvasive neoplasias in two mouse models of DCIS.

MATERIALS AND METHODS

Animals

All procedures were carried out in accordance with our institution's Animal Care and Use Committee approval. Twenty-two mice from commonly utilized xenograft (n=5) and GEMM (n=17) models of DCIS were selected. In MCF10DCIS xenograft mice, human cells were injected into the inguinal mammary gland #4 of 8-10 week old athymic nude mice and DCIS-like lesions developed after ~3 weeks (Miller et al., 2000, Hu et al., 2008). In the C3(1) SV40 Tag GEMM, mammary intraepithelial neoplasia (MIN), an analog to human DCIS, developed at ~12 weeks of age while invasive ductal carcinoma developed by ~16 weeks of age (Green et al., 2000, Maroulakou et al., 1994). Animals were anesthetized prior to imaging experiments, and anesthesia was maintained during imaging at 1.5% isoflorane. The temperature, heart rate and respiration rate were monitored with data taken every minute, and the respiration rate was used to obtain gated images when necessary. All four inguinal mammary glands were imaged, numbered #4,5 (left side), and #9,10 (right side). Glands #4 and #9 extend from the intramammary lymph node to the spine, and will be referred to as the *posterior inguinal* glands. Glands #5 and #10 extend down the belly of the animal, and will be referred to as the *anterior inguinal* glands (Figure 1).

Imaging protocols and co-registration

The experimental workflow is illustrated in Figure 1, consisting of preparation and placement of the agar grid, MRI, MRI-directed ultrasound, and euthanization for subsequent tissue processing and histological evaluation.

Agar grid: A fine polyethylene mesh ~ 65 mm × 30 mm in size with 3 mm spacing was embedded in partially deuterated agar and wrapped around each mouse during imaging. Using Sharpie markers, the grid edges were marked on the skin of the mouse. In prior work, this grid has been shown to produce a two-dimensional coordinate system on MRI that allows for correlation with histology (Jansen et al., 2008)

and for registration of serial MRI scans (Jansen et al., 2009a). In the present study, the agar grid was used to co-register MRI with ultrasound and histology.

MRI protocols: Imaging was performed on a 3.0T Philips Achieva scanner.   Mice were positioned in a volume coil so that the inguinal intramammary lymph nodes were in the center of the coil. Initially, a T_1 weighted acquisition with fat suppression was performed (T_1 FFE, 3D, TR/TE 26/2.9ms, in plane resolution=0.2 mm, slice thickness=0.4 mm, field of view (FOV)=30×20×9 mm, number of excitations (NEX)=8, flip angle (FA)=25°, no respiratory gating) followed by a T_2 weighted scan with fat suppression (T_2 TSE, 2D, TR/TE=4000/65 ms, in plane resolution = 0.17 mm, slice thickness=0.5 mm, FOV=30×30×12 mm, NEX=2, number of slices =24, with respiratory gating). On a subset of n=9 C3(1) SV40 Tag mice, dynamic contrast enhanced MRI (DCEMRI) (T_1 FFE DCE, 3D, TR/TE=13/3ms, in plane resolution =0.23 mm, slice thickness=1.0 mm, NEX=2, FA=20°, temporal resolution= 17 secs, duration =17 min 42 sec, no respiratory gating) was obtained before, during and after a single-dose injection of gadopentetate dimeglumine (Magnevist; Berlex, Wayne, NJ) via a tail vein catheter at a dose of 0.2 mmol/kg.

MRI-directed ultrasound: Ultrasound was subsequently performed to further evaluate MR findings. To correlate MRI and ultrasound, the grid coordinates of MRI-detected lesions were noted on the MRI, and then transferred to the skin of the mouse (Figure 1). These skin markings were subsequently used to guide placement of a 40 MHz ultrasound transducer for the acquisition of B-mode images on a Vevo2100 imaging system (VisualSonics Inc, Toronto Canada).

Correlation of MRI with histology

To evaluate the sensitivity of MRI and ultrasound methods for detecting preinvasive lesions, hematoxylin and eosin (H&E) stained sections of imaged mammary glands were obtained (5-micron thick H&E sections every 50 microns) and evaluated by a veterinary pathologist (MA). Each gland (#4,5,9,10) was separately classified into one of four categories: (i) normal, (ii) preinvasive carcinoma with/without microinvasion, (iii) invasive and preinvasive carcinoma, and (iv) predominantly invasive carcinoma.   MR

images were reviewed by a post-doctoral fellow (SAJ) with 6 years of experience analyzing MRI of the mouse mammary gland, and each gland (#4,5,9,10) was classified into the same categories, using the morphologic descriptors *nonmass* and *mass* to identify preinvasive and invasive regions, respectively (Jansen et al., 2009a, Jansen et al., 2008). The MRI assessment was blinded to the pathological assessment. MR images were spatially correlated with H&E sections using the agar grid as detailed in prior work (Jansen et al., 2008) and the sensitivity of MRI was calculated using the histologic evaluation as the reference standard. Sensitivity was compared in the posterior and anterior inguinal glands to determine regional variability in the efficacy of MRI.

Image Analysis

mBIRADS: T_1 FFE images were analyzed according to an adapted version of the human BIRADS lexicon (ACR, 2003), referred to as the mouse BIRADS or mBIRADS lexicon. Initially the *type* of the lesion was classified as 'mass' or 'nonmass'. Prior work has shown that the 'nonmass' descriptor reliably identifies preinvasive lesions in the C3(1) SV40 Tag model (Jansen et al., 2008). For nonmass lesions, additional descriptors were the *distribution* ('linear', 'ductal' or 'segmental') and the *pattern* ('homogeneous', 'clumped' or 'stippled').

SNR and CNR. All data analysis was performed using software written in IDL (Research Systems, Inc., Boulder, CO, USA). A postdoctoral fellow (SAJ) with six years of experience analyzing MRI of preinvasive and invasive mammary cancers traced the following regions of interest (ROI), confirmed by the histologic evaluation: invasive carcinoma, preinvasive carcinoma, lymph node, normal mammary gland (NMG) and muscle. The signal-to-noise ratio (SNR) and the contrast-to-noise ratio (CNR) relative to NMG tissue and muscle were calculated on T_1 FFE and T_2 TSE as follows:

$$SNR = \bar{S}/\sigma_{noise} \qquad CNR_{NMG} = SNR_{ROI} - SNR_{NMG} \qquad CNR_{muscle} = SNR_{ROI} - SNR_{muscle}$$

where $\bar{S}$ is the average signal intensity in the ROI and σ_{noise} was averaged from the standard deviations of signal intensities measured in a 5×5 mm ROI drawn in the corners of the image.

Contrast kinetics. Signal intensity vs. time, or kinetic, curves were generated from T_1 FFE DCE data by manually tracing an ROI around lesions. These curves were analyzed qualitatively and classified as persistent, plateau or washout as described by the BIRADS lexicon (ACR, 2003). In addition, two compartment pharmacokinetic modeling was performed and parameters K^{trans} and v_e calculated, using software as described previously (Turkbey et al., 2010).

Statistical analysis

The SNR, CNR_{NMG} and CNR_{muscle} of lymph nodes, invasive and preinvasive carcinomas on T_1 FFE and T_2 TSE pulse sequences were compared using the Student's *t*-test. The sensitivity of MRI and MRI-directed ultrasound in the posterior vs. anterior inguinal glands was compared using the Fishers exact test. For both tests, a *p* value < 0.05 was considered to be statistically significant.

RESULTS

Images of preinvasive cancers from representative GEMM and xenograft mice are shown in Figure 2. The MIN lesions in C3(1) mice arise *de novo* within an intact mammary fat pad, surrounded by normal tissue. Conversely, DCIS arising in MCF10DCIS mice appears as larger palpable lesions that are not embedded within an intact mammary gland. Given that the imaging presentation of human DCIS is more akin to the GEMM, i.e., a typically nonpalpable lesion embedded in the normal breast, the remainder of our analysis was focused on MIN lesions in C3(1) SV40 Tag mice.

A total of 60 MIN lesions were histologically confirmed, of which MRI detected 53 for an overall sensitivity of 88% (53/60). The sensitivity of MRI was higher in the posterior inguinal glands compared to the anterior inguinal glands, although this difference was not statistically significant ($p > 0.2$). Similarly, the sensitivity of MRI-directed ultrasound was significantly higher in the posterior glands, at 97%, compared to the anterior inguinal glands, at 37% ($p < 0.0001$) (Table 1).

Qualitative analysis (Table 2) of lesion morphology according to the mBIRADS lexicon revealed that the predominant distribution of nonmass MIN lesions was segmental, with a homogeneous pattern. Quantitatively (Figure 3), MIN lesions presented with a significantly higher SNR than NMG on T_1 FFE (at 35±7 vs. 18±2, respectively) and T_2 TSE (at 29±8 vs. 13±3, respectively) ($p < 0.0001$), and a significantly lower SNR compared to lymph nodes and invasive tumors ($p < 0.001$). Although MIN lesions exhibited higher SNR on T_1 FFE than on T_2 TSE ($p < 0.0002$), both MIN and invasive tumors achieved comparable CNR_{NMG} on T_1 and T_2 weighted acquisitions ($p > 0.2$) and significantly higher CNR_{muscle} on T_2 TSE ($p < 0.0001$). DCEMRI was obtained for 15/53 MRI-detected MIN lesions. Analysis of kinetic curve shape demonstrated that 20% (3/15) exhibited minimal enhancement, while 47% (7/15) displayed a plateau curve shape and 20% (3/15) a washout curve shape. For the n=12 enhancing MIN, the average K^{trans} and v_e values were 0.11±0.09 min^{-1} and 0.47 ±0.22, respectively.

DISCUSSION

Our results suggest that from an imaging perspective the C3(1) SV40 Tag GEMM more faithfully mimics human DCIS compared to the commonly used MCF10DCIS xenograft model. In GEMMs, preinvasive cancers arise stochastically within pre-existing mammary ducts and are surrounded by the mammary gland microenvironment including an intact immune system. Although intramammary fat pad injections of MCF10DCIS cells did not achieve this phenotype, recently developed xenograft models may do so. For example, DCIS patient-derived cells that are injected directly into the murine ductal system via the nipple may prove to be more effective models of DCIS (Valdez et al., 2011, Behbod et al., 2009).

Previous studies have shown that on small bore small animal imaging systems at high magnetic field strength (4.7 T and 9.4 T), it is possible to detect preinvasive cancers in transgenic mice using a proton density/moderately T_1 weighted pulse sequence (Gradient Recalled Echo, TR/TE ~1000/5.5 ms) (Jansen et al., 2008, Jansen et al., 2011). Our study complements this prior work in several important ways. We have implemented pulse sequences that are more similar to clinically acquired T_1 and T_2 weighted breast MRI, on a 3T clinical MRI scanner. In doing so, we have established a new T_1 weighted fast-field echo imaging approach for preinvasive murine neoplasias that matches or exceeds the sensitivity, SNR and CNR_{NMG} of prior techniques, in half the imaging time. Finally, we found that the CNR_{NMG} of preinvasive neoplasia on T_2 TSE was comparable to T_1 FFE, whereas in prior studies T_2 weighting was not reported to be as effective (Jansen et al., 2008).

Human DCIS is typically detected with T_1 FFE after the administration of a gadolinium-chelated based contrast agent (Kuhl et al., 2007). Conversely, we have found that murine MIN can be visualized on T_1 FFE and T_2 TSE with high CNR_{NMG} without contrast medium. The mechanisms responsible for this important discrepancy are not clear. Given the likelihood that the magnetic properties of neoplastic epithelial cells/ducts may be similar in mice and women at 3T, it may be differences in the tumor microenvironment that yield a different imaging phenotype. For example, neoplastic ducts in the mouse are distributed sparsely within a fat pad, whereas in women they may be in close proximity with normal TDLUs embedded within an intralobular stroma. In performing a contrast kinetic characterization of

MIN lesions at 3T we found some qualitative and quantitative similarities with human disease, including exhibiting a predominantly plateau or washout curve shape (Jansen et al., 2007) and comparable values of K^{trans} and v_e (Furman-Haran et al., 2005). However, our DCEMRI methods were limited and further improvements are required, including increased population size and temporal resolution, to better compare the contrast enhanced phenotype of murine and human preinvasive neoplasias.

Molecular and metabolic imaging is highly desirable to better reveal biological diversity in mouse models of DCIS. Indeed, in previous work by Abbey et al, FDG-PET imaging was used to characterize metabolic changes during breast cancer progression in an allograft mouse model of DCIS (Abbey et al., 2004, Abbey et al., 2006). However, molecular imaging techniques often suffer from poor spatial resolution and anatomic localization, and could thus benefit from concomitant anatomic imaging for lesion detection and localization. Our results set the stage for such an approach, as we have established rapid, high resolution and highly sensitive anatomic imaging techniques in two different modalities, MRI and ultrasound. Furthermore, in carefully mapping out the lesions in this study, we found improved sensitivity in the posterior inguinal glands compared to anterior inguinal glands, likely due to partial volume effects near the belly of the mouse.

For multimodality imaging it is also essential to develop co-registration methods that can accurately correlate diverse images with one another other and with histology. This is particularly relevant for small preinvasive mammary cancers that are not palpable or visible. Prior work in MRI-ultrasound correlation has been developed for palpable lesions. For example Loveless et al. developed an iterative closest point algorithm method to co-register MRI and ultrasound images using palpable tumors ($\sim$100mm^3) arising in a xenograft model of breast cancer(Loveless et al., 2009). The novel approach we have established in this study utilizes the agar grid as a two dimensional coordinate system that can accurately co-register *in vivo* images and histology of sub-millimeter cancers.

Ultimately we are interested in investigating the capacity for image-based biomarkers to identify molecular or prognostic subtypes of human DCIS, using GEMMs as a model system. In this study, we have added to the imaging toolkit that can be used to characterize murine preinvasive neoplasia by

developing new clinically relevant MRI techniques at 3 Tesla, adding ultrasound characterization and establishing a new multi-modality correlation strategy. In future work, application of more advanced imaging techniques, such as diffusion weighted MRI and contrast enhanced ultrasound, can yield additional quantitative measures of lesion biology and physiology. However, in addition to improved imaging techniques it is also essential to utilize more diverse GEMMs of DCIS. Imaging investigations of murine MIN have been limited to models wherein viral proteins (e.g., SV40 Tag (Jansen et al., 2008, Jansen et al., 2011, Jansen et al., 2009b) and PyMT (Abbey et al., 2006, Namba et al., 2006, Abbey et al., 2004)) induce aggressive tumorigenesis by concurrently altering several molecular pathways (Green et al., 2000). However, these models do not capture the full complexity of human DCIS. More advanced GEMMs can target individual pathways known to be altered in DCIS, including Rb (Simin et al., 2004), HER2 (Moody et al., 2002) and PTEN (Dourdin et al., 2008) in a cell type and temporally controlled manner. It is by combining advanced imaging approaches with sophisticated mouse modeling techniques that insights on image-based biomarkers of DCIS are likely to follow.

TABLES

Table 1: Sensitivity of MRI and MRI-directed ultrasound for MIN in different gland regions of C3(1) SV40 Tag mice.

	Number of MIN histologically	Sensitivity of MRI	Sensitivity of MRI-directed ultrasound
All inguinal glands	60	88% (53/60)	72% (38/53)
Posterior inguinal glands	33	94% (31/33)	97% (30/31)
Anterior inguinal glands	27	82% (22/27)	36% (8/22)

Table 2: Qualitative mBIRADS features for MIN lesions in C3(1) SV40 Tag mice.

		MIN No. (%)
Type	Mass	0 (0)
	Nonmass	53 (100)
Distribution	Linear	15 (28)
	Ductal	11 (21)
	Segmental	27 (51)
Pattern	Homogeneous	23 (43)
	Stippled	20 (38)
	Clumped	10 (19)

FIGURE CAPTIONS

Figure 1. Multimodality imaging workflow. **A.** Initially, the agar grid is wrapped around the mouse and grid edge positions marked on the skin of the mouse**. B**. MRI of one axial cross-section through the mouse (dotted line from A) revealing an intramammary lymph node (red arrow). The agar grid can be seen on MRI (arrows) and thus the grid coordinates of the lymph node noted. **C**. After removing the mouse from the imaging coil, the location of the MRI detected lesion is marked on the skin of the mouse to guide placement of the ultrasound transducer. **D**. Ultrasound imaging is performed to locate and evaluate the MRI-detected lesion. **E.** Finally, the animal is euthanized and glands are excised for histological analysis. Shown are the posterior inguinal glands #4 and 9 (outlined in blue), the anterior inguinal glands #5 and #10 (outlined in black) and the intramammary lymph nodes circled in orange.

Figure 2. Representative noncontrast T_1 FFE, T_2 TSE, ultrasound and H&E images from a normal gland (top row), MIN lesion in the C3(1) SV40 Tag GEMM (middle row, thin arrows) and DCIS lesion in the MCF10DCIS xenograft model (bottom row, thin arrows). Intramammary lymph nodes are identified by arrowheads, while an invasive tumor (middle row) is indicated with a gray arrow.

Figure 3. The SNR, CNR_{NMG} and CNR_{muscle} of lymph nodes, MIN and invasive tumors in C3(1) SV40 Tag mice on noncontrast T_1 FFE and T_2 TSE acquisitions.

Figure 1. Example multimodality imaging workflow. **A.** Initially, the agar grid is wrapped around the mouse and grid edge positions marked on the skin of the mouse. **B**. MRI of one axial cross-section through the mouse (dotted line from A) revealing an intramammary lymph node (red arrow). Because the agar grid is MR-visible, the grid coordinates of the lymph node are noted. **C**. After removing the mouse from the imaging coil, the location of the MRI detected lesion is marked on the skin of the mouse to guide placement of the ultrasound transducer. **D**. Ultrasound imaging is performed to locate and evaluate the MRI-detected lesion. **E**. Finally, the animal is euthanized and glands are excised for histological analysis. Shown are the posterior inguinal glands #4 and 9 (outlined in blue), the anterior inguinal glands #5 and #10 (outlined in black) and the intramammary lymph nodes circled in white.
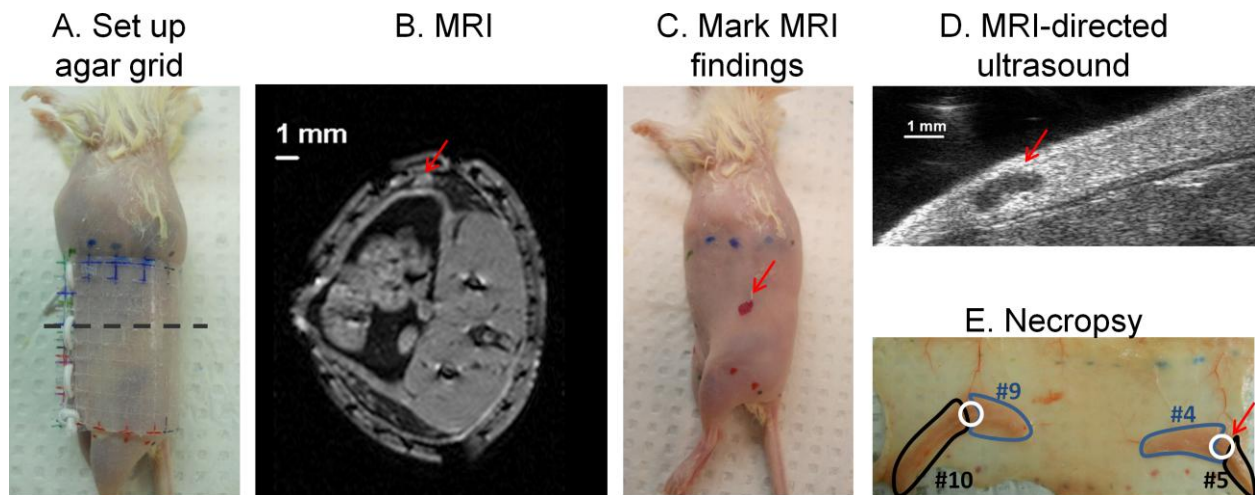
Figure 2. Representative noncontrast T_1 FFE, T_2 TSE, ultrasound and H&E images from a normal gland (top row), MIN lesion in the C3(1) SV40 Tag GEMM (middle row, thin arrows) and DCIS lesion in the MCF10DCIS xenograft model (bottom row, thin arrows). Intramammary lymph nodes are identified by arrowheads.
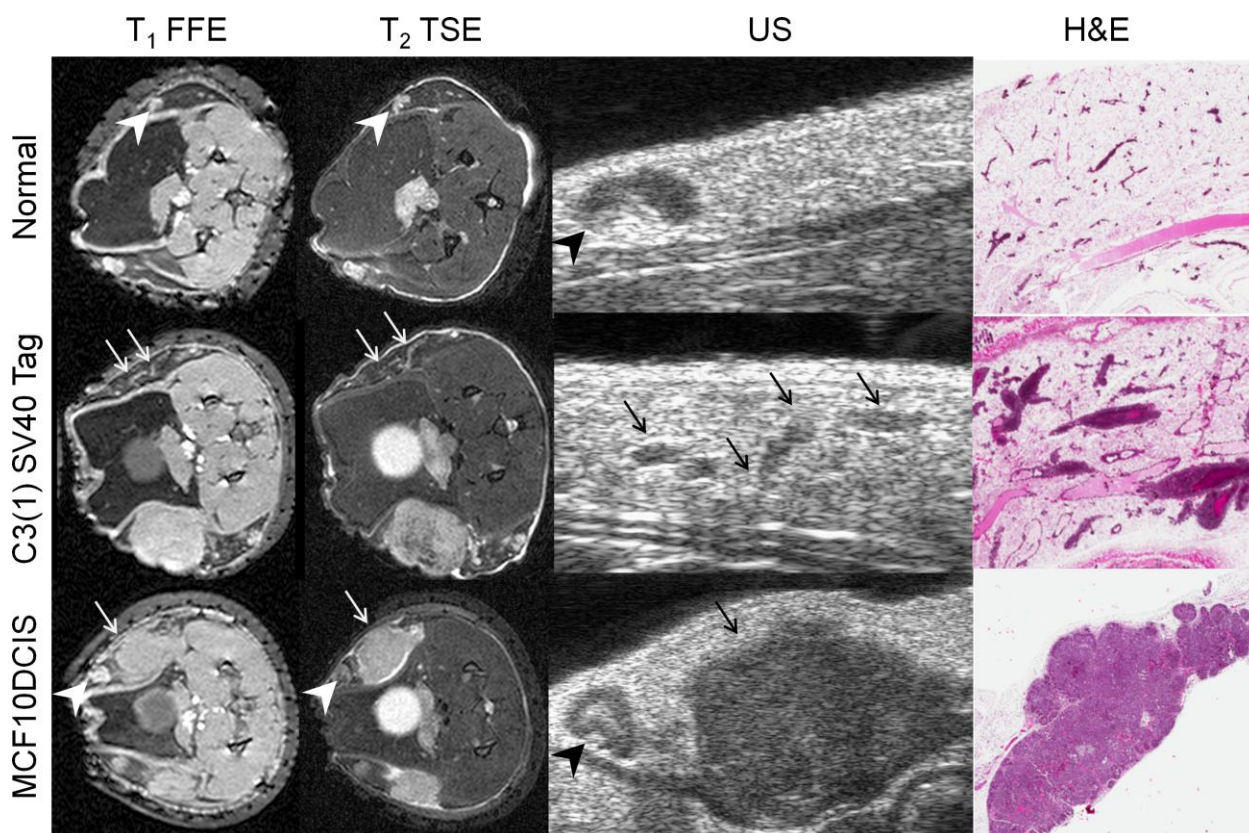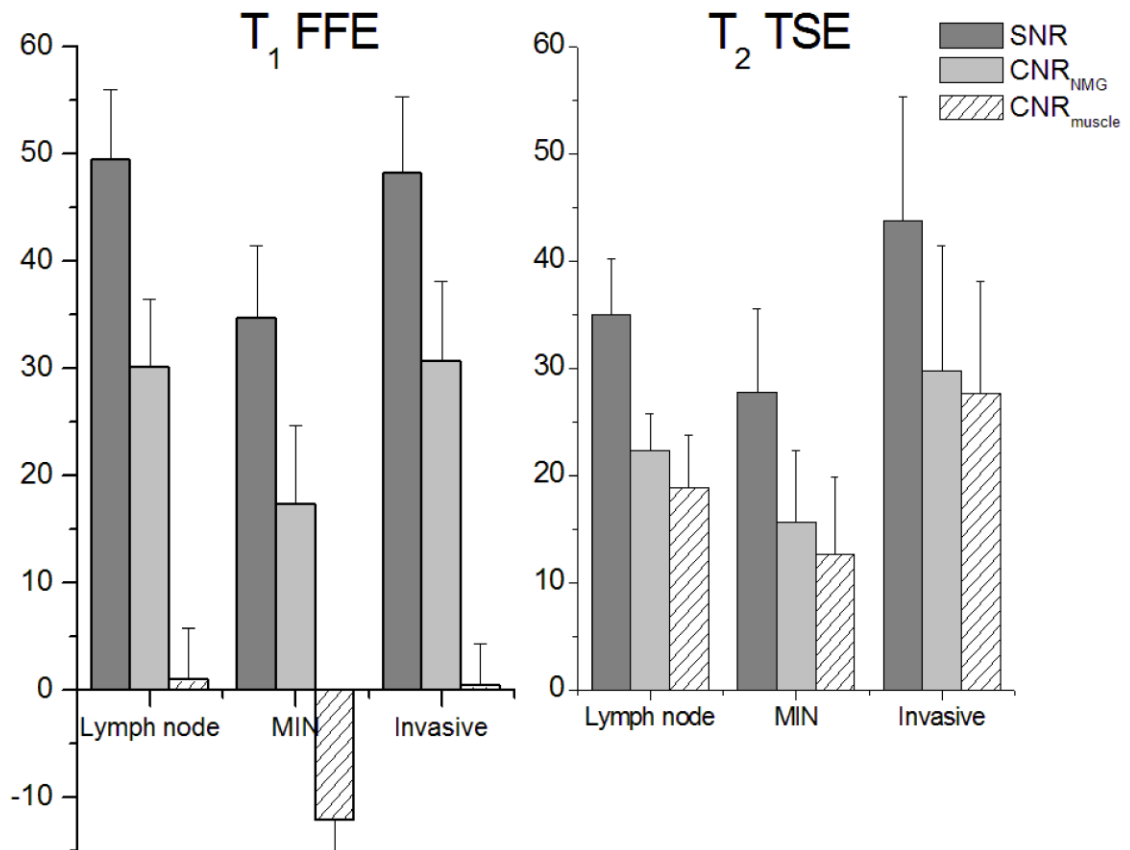
Figure 3. The SNR, CNR_{NMG} and CNR_{muscle} of lymph nodes, MIN and invasive tumors in C3(1) SV40

Tag mice on T_1 FFE and T_2 TSE acquisitions.

REFERENCES

Abbey C K, Borowsky A D, Gregg J P, Cardiff R D and Cherry S R 2006 Preclinical imaging of mammary intraepithelial neoplasia with positron emission tomography *Journal of mammary gland biology and neoplasia* **11** 137-49.

Abbey C K, Borowsky A D, Mcgoldrick E T, Gregg J P, Maglione J E, Cardiff R D and Cherry S R 2004 In vivo positron-emission tomography imaging of progression and transformation in a mouse model of mammary neoplasia *Proceedings of the National Academy of Sciences of the United States of America* **101** 11438-43.

Abe H, Schmidt R A, Shah R N, Shimauchi A, Kulkarni K, Sennett C A and Newstead G M 2010 MR-directed ("Second-Look") ultrasound examination for breast lesions detected initially on MRI: MR and sonographic findings *AJR. American journal of roentgenology* **194** 370-7.

ACR 2003. *American College of Radiology: ACR Breast Imaging Reporting and Data System Atlas (BI-RADS).* Reston, VA.

Allegra C J, Aberle D R, Ganschow P, Hahn S M, Lee C N, Millon-Underwood S, Pike M C, Reed S D, Saftlas A F, Scarvalone S A, Schwartz A M, Slomski C, Yothers G and Zon R 2010 National Institutes of Health State-of-the-Science Conference statement: Diagnosis and Management of Ductal Carcinoma In Situ September 22-24, 2009 *Journal of the National Cancer Institute* **102** 161-9.

Allred D C 2010 Ductal carcinoma in situ: terminology, classification, and natural history *Journal of the National Cancer Institute. Monographs* **2010** 134-8.

Behbod F, Kittrell F S, Lamarca H, Edwards D, Kerbawy S, Heestand J C, Young E, Mukhopadhyay P, Yeh H W, Allred D C, Hu M, Polyak K, Rosen J M and Medina D 2009 An intraductal human-in-mouse transplantation model mimics the subtypes of ductal carcinoma in situ *Breast cancer research : BCR* **11** R66.

Cho N, Moon W K, Chang J M, Yi A, Koo H R, Park J S and Park I A 2011 Sonoelastographic lesion stiffness: preoperative predictor of the presence of an invasive focus in nonpalpable DCIS diagnosed at US-guided needle biopsy *European radiology* **21** 1618-27.

D'orsi C J 2010 Imaging for the diagnosis and management of ductal carcinoma in situ *Journal of the National Cancer Institute. Monographs* **2010** 214-7.

Dourdin N, Schade B, Lesurf R, Hallett M, Munn R J, Cardiff R D and Muller W J 2008 Phosphatase and tensin homologue deleted on chromosome 10 deficiency accelerates tumor induction in a mouse model of ErbB-2 mammary tumorigenesis *Cancer research* **68** 2122-31.

Erbas B, Provenzano E, Armes J and Gertig D 2006 The natural history of ductal carcinoma in situ of the breast: a review *Breast cancer research and treatment* **97** 135-44.

Furman-Haran E, Schechtman E, Kelcz F, Kirshenbaum K and Degani H 2005 Magnetic resonance imaging reveals functional diversity of the vasculature in benign and malignant breast lesions *Cancer* **104** 708-18.

Green J E, Shibata M A, Yoshidome K, Liu M L, Jorcyk C, Anver M R, Wigginton J, Wiltrout R, Shibata E, Kaczmarczyk S, Wang W, Liu Z Y, Calvo A and Couldrey C 2000 The C3(1)/SV40 T-antigen transgenic mouse model of mammary cancer: ductal epithelial cell targeting with multistage progression to carcinoma *Oncogene* **19** 1020-7.

Hu M, Yao J, Carroll D K, Weremowicz S, Chen H, Carrasco D, Richardson A, Violette S, Nikolskaya T, Nikolsky Y, Bauerlein E L, Hahn W C, Gelman R S, Allred C, Bissell M J, Schnitt S and Polyak K 2008 Regulation of in situ to invasive breast carcinoma transition *Cancer cell* **13** 394-406.

Jansen S A 2011 Ductal carcinoma in situ: detection, diagnosis, and characterization with magnetic resonance imaging *Semin Ultrasound CT MR* **32** 306-18.

Jansen S A, Conzen S D, Fan X, Krausz T, Zamora M, Foxley S, River J, Newstead G M and Karczmar G S 2008 Detection of in situ mammary cancer in a transgenic mouse model: in vitro and in vivo

MRI studies demonstrate histopathologic correlation *Physics in medicine and biology* **53** 5481-93.

Jansen S A, Conzen S D, Fan X, Markiewicz E, Krausz T, Newstead G M and Karczmar G S 2011 In vivo MRI of early stage mammary cancers and the normal mouse mammary gland *NMR in biomedicine* **24** 880-7.

Jansen S A, Conzen S D, Fan X, Markiewicz E J, Newstead G M and Karczmar G S 2009a Magnetic resonance imaging of the natural history of in situ mammary neoplasia in transgenic mice: a pilot study *Breast cancer research : BCR* **11** R65.

Jansen S A, Newstead G M, Abe H, Shimauchi A, Schmidt R A and Karczmar G S 2007 Pure ductal carcinoma in situ: kinetic and morphologic MR characteristics compared with mammographic appearance and nuclear grade *Radiology* **245** 684-91.

Jansen S A, Paunesku T, Fan X, Woloschak G E, Vogt S, Conzen S D, Krausz T, Newstead G M and Karczmar G S 2009b Ductal carcinoma in situ: X-ray fluorescence microscopy and dynamic contrast-enhanced MR imaging reveals gadolinium uptake within neoplastic mammary ducts in a murine model *Radiology* **253** 399-406.

Kerlikowske K 2010 Epidemiology of ductal carcinoma in situ *Journal of the National Cancer Institute. Monographs* **2010** 139-41.

Kuhl C K, Schrading S, Bieling H B, Wardelmann E, Leutner C C, Koenig R, Kuhn W and Schild H H 2007 MRI for diagnosis of pure ductal carcinoma in situ: a prospective observational study *Lancet* **370** 485-92.

Lari S A and Kuerer H M 2011 Biological Markers in DCIS and Risk of Breast Recurrence: A Systematic Review *Journal of Cancer* **2** 232-61.

Loveless M E, Whisenant J G, Wilson K, Lyshchik A, Sinha T K, Gore J C and Yankeelov T E 2009 Coregistration of ultrasonography and magnetic resonance imaging with a preliminary investigation of the spatial colocalization of vascular endothelial growth factor receptor 2 expression and tumor perfusion in a murine tumor model *Molecular imaging* **8** 187-98.

Maroulakou I G, Anver M, Garrett L and Green J E 1994 Prostate and mammary adenocarcinoma in transgenic mice carrying a rat C3(1) simian virus 40 large tumor antigen fusion gene *Proceedings of the National Academy of Sciences of the United States of America* **91** 11236-40.

Miller F R, Santner S J, Tait L and Dawson P J 2000 MCF10DCIS.com xenograft model of human comedo ductal carcinoma in situ *Journal of the National Cancer Institute* **92** 1185-6.

Moody S E, Sarkisian C J, Hahn K T, Gunther E J, Pickup S, Dugan K D, Innocent N, Cardiff R D, Schnall M D and Chodosh L A 2002 Conditional activation of Neu in the mammary epithelium of transgenic mice results in reversible pulmonary metastasis *Cancer cell* **2** 451-61.

Namba R, Young L J, Abbey C K, Kim L, Damonte P, Borowsky A D, Qi J, Tepper C G, Macleod C L, Cardiff R D and Gregg J P 2006 Rapamycin inhibits growth of premalignant and malignant mammary lesions in a mouse model of ductal carcinoma in situ *Clinical cancer research : an official journal of the American Association for Cancer Research* **12** 2613-21.

Simin K, Wu H, Lu L, Pinkel D, Albertson D, Cardiff R D and Van Dyke T 2004 pRb inactivation in mammary cells reveals common mechanisms for tumor initiation and progression in divergent epithelia *PLoS biology* **2** E22.

Turkbey B, Pinto P A, Mani H, Bernardo M, Pang Y, Mckinney Y L, Khurana K, Ravizzini G C, Albert P S, Merino M J and Choyke P L 2010 Prostate cancer: value of multiparametric MR imaging at 3 T for detection--histopathologic correlation *Radiology* **255** 89-99.

Valdez K E, Fan F, Smith W, Allred D C, Medina D and Behbod F 2011 Human primary ductal carcinoma in situ (DCIS) subtype-specific pathology is preserved in a mouse intraductal (MIND) xenograft model *The Journal of pathology* **225** 565-73.

Van Dyke T and Jacks T 2002 Cancer modeling in the modern era: progress and challenges *Cell* **108** 135-44.